Check for updates

Bulk Incorporation with 4-Methylphenethylammonium Chloride for Efficient and Stable Methylammonium-Free Perovskite and Perovskite-Silicon Tandem Solar Cells

The Duong, Thuan Nguyen, Keqing Huang, Huyen Pham, Sunita Gautam Adhikari, Motiur Rahman Khan, Leiping Duan, Wensheng Liang, Kean Chern Fong, Heping Shen, Anh Dinh Bui, Azul Osorio Mayon, Thien Truong, Grace Tabi, Viqar Ahmad, Sachin Surve, Jingnan Tong, Teng Kho, Thanh Tran-Phu, Teng Lu, Jianghui Zheng, Ulrich W. Paetzold, Uli Lemmer, Anita Ho Baillie, Yun Liu, Gunther Andersson, Thomas White, Klaus Weber, and Kylie Catchpole*

Methylammonium (MA)-free perovskite solar cells have the potential for better thermal stability than their MA-containing counterparts. However, the efficiency of MA-free perovskite solar cells lags behind due to inferior bulk quality. In this work, 4-methylphenethylammonium chloride (4M-PEACl) is added into a MA-free perovskite precursor, which results in greatly enhanced bulk quality. The perovskite crystal grains are significantly enlarged, and defects are suppressed by a factor of four upon the incorporation of an optimal concentration of 4M-PEACl. Quasi-2D perovskites are formed and passivate defects at the grain boundaries of the perovskite crystals. Furthermore, the perovskite surface chemistry is modified, resulting in surface energies more favorable for hole extraction. This facile approach leads to a steady state efficiency of 23.7% (24.2% in reverse scan, 23.0% in forward scan) for MA-free perovskite solar cells. The devices also show excellent light stability, retaining more than 93% of the initial efficiency after 1000 h of constant illumination in a nitrogen environment. In addition, a four-terminal mechanically stacked perovskite-silicon tandem solar cell with champion efficiency of 30.3% is obtained using this MA-free composition. The encapsulated tandem devices show excellent operational stability, retaining more than 98% of the initial performance after 42 day/night cycles in an ambient atmosphere.

1. Introduction

Perovskite solar cell technology has emerged in recent years to reach an unprecedented efficiency of 25.7%,[1] approaching the record efficiency of silicon solar cells at 26.7%.[2] Perovskite cells can also be combined with the existing silicon technology in tandem configurations to achieve ultrahigh efficiency. The efficiency of the best 2-terminal monolithic perovskite-silicon double-junction tandem cell has reached 31.25%, while the highest efficiency for a 4-terminal perovskite-silicon double-junction tandem is 30.24%.[3] Most state-of-the-art single-junction perovskite solar cells have a n-i-p structure and use formamidinium lead triiodide ($FAPbI_3$) perovskite composition because of its narrow bandgap (1.48 eV) which is closer to the ideal bandgap for single junction solar cells,[4] and its excellent thermal stability compared to methylammonium (MA)—based perovskites.[5]

T. Duong, T. Nguyen, K. Huang, L. Duan, W. Liang, K. C. Fong, H. Shen, A. D. Bui, A. O. Mayon, T. Truong, G. Tabi, V. Ahmad, S. Surve, J. Tong, T. Kho, T. White, K. Weber, K. Catchpole
School of Engineering
The Australian National University
Canberra 2601, Australia
E-mail: the.duong@anu.edu.au

The ORCID identification number(s) for the author(s) of this article can be found under https://doi.org/10.1002/aenm.202203607.

© 2023 The Authors. Advanced Energy Materials published by Wiley-VCH GmbH. This is an open access article under the terms of the Creative Commons Attribution-NonCommercial-NoDerivs License, which permits use and distribution in any medium, provided the original work is properly cited, the use is non-commercial and no modifications or adaptations are made.

DOI: 10.1002/aenm.202203607

H. Pham
Department of Materials Science and Engineering
Monash University
Victoria 3800, Australia

S. G. Adhikari, G. Andersson
Flinders Institute for Nanoscale Science and Technology
Flinders University
Adelaide, South Australia 5042, Australia

S. G. Adhikari, G. Andersson
Flinders Microscopy and Microanalysis
College of Science and Engineering
Flinders University
Adelaide, South Australia 5042, Australia

M. R. Khan, U. W. Paetzold, U. Lemmer
Light Technology Institute
Karlsruhe Institute of Technology
Engesserstrasse 13, 76131 Karlsruhe, Germany

16146840, 0, Downloaded from https://onlinelibrary.wiley.com/doi/10.1002/aenm.202203607 by Karlsruher Inst F. Technologie, Wiley Online Library on [27/01/2023]. See the Terms and Conditions (https://onlinelibrary.wiley.com/terms-and-conditions) on Wiley Online Library for rules of use; OA articles are governed by the applicable Creative Commons License

However, due to the slightly larger ionic size of the FA cation (253 pm) compared to the MA cation (217 pm), there is a distortion of the lattice structure of the 3D perovskites. Therefore, pure $FAPbI_3$ is in a photoinactive yellow phase at room temperature.[6] To obtain the photoactive black $FAPbI_3$ phase and improve the perovskite crystallinity, a large amount of methylammonium chloride (MACl) up to 40 mol% was added to the $FAPbI_3$ precursor as the additive in most record devices.[1,7] Although majority of the MA evaporates during the annealing step, some residual MA of up to 5% can remain.[7f] This could potentially lead to thermal instability since previous reports showed that MA outgases at temperatures as low as 85 °C.[8] To circumvent this, Park et al. first pioneered the hybridization of FA and Cs and successfully demonstrated MA-free perovskite solar cells with excellent stability and an efficiency of 19%.[6] Saliba et al. demonstrated the incorporation of a smaller cation, Rb, into the FA/Cs perovskites and improved the device efficiency to 20.35%.[9] However, Rb can induce other instability issues related to moisture,[10] and light and heat,[11] which are undesirable for the commercialization of perovskite technology. Many groups have investigated surface passivation as a promising approach to improve the efficiency of MA-free perovskite solar cells such as using fullerene passivators,[12] ammonium salts,[13] Lewis base ligand,[14] and fluoroarene anchored functional material.[15] Other strategies have also been used to improve the bulk of MA-free perovskite compositions such as lead-halide-templated crystallization with the addition of N-methyl-2-pyrrolidone solvent,[16] and the use of additives, for example, conductive polymers,[17] and organic dyes.[18] In this work, we incorporated 4-methylphenethylammonium chloride (4M-PEACl), a new derivative of phenethylammonium salt known to form 2D perovskites, into the MA-free perovskite precursors to enhance the bulk quality of the perovskite films. The resultant perovskite bandgap is 1.55 eV, which is close to that of the $FAPbI_3$. For single junction device demonstration, a champion efficiency of 24.2% (reverse scan)/23.0% (forward scan) and a steady state performance of 23.7% was achieved for MA-free n-i-p perovskite solar cells with excellent light stability for 1000 h. Our devices were also used in the demonstration of 4-terminal perovskite-silicon double-junction tandem solar cells. The advantage of the 4-terminal tandem is a larger range of perovskite bandgaps that can be used for the top cell without significantly affecting the overall performance as there is no requirement for current-matching, otherwise needed in the 2-terminal tandem configuration. The current matching requirement in 2-terminal tandem devices leads to the use of mixed-halides I/Br perovskite top cells with relatively wider bandgaps (1.68–1.72 eV),[19] causing light instability due to light-induced halide phase segregation.[20] Using our developed perovskite cells in the 4-terminal perovskite-silicon tandem configuration, we achieved an efficiency of 30.3%, which is one of the highest efficiencies reported for this type of device. Importantly, the encapsulated 4-terminal perovskite-silicon tandem cells showed excellent operational stability, retaining over 98% of the initial performance after 42 day/night cycles in ambient.

2. Results and Discussion

2.1. Effect of 4-Methylphenethylammonium Chloride Incorporation on the Morphology, Crystal Structure, and New Phase Formation of Perovskite Films

We first used scanning electron microscopy (SEM) and transmission electron microscopy (TEM) to investigate the effect of incorporating 4M-PEACl into 3D perovskite bulk on the perovskite microstructure including surface morphology, grain size, crystal structure, and defects. The 3D perovskite films were prepared following our previous report, containing $FAPbI_3$ and 10% of CsCl.[21] Different concentrations (2% and 5% mol ratio) of 4M-PEACl incorporated into the 3D perovskite were studied, which are abbreviated as $x = 0.02$ and $x = 0.05$, respectively. **Figure 1**A–C compare the polycrystalline perovskite films before (reference) and after 4M-PEACl incorporation ($x = 0.02$ and $x = 0.05$). The average perovskite crystal size in the reference sample was around 425 nm while the $x = 0.02$ perovskite film produced significantly larger crystal grains with an average size of around 877 nm and the $x = 0.05$ perovskite film had a slightly smaller average grain size of around 748 nm, still significantly larger than that of the reference sample. Perovskite crystallization process generally contains nucleation process and crystal growth process. The nucleation process can be divided into homogeneous and heterogeneous nucleation.[22] Heterogeneous nucleation occurs at preferential sites including phase boundaries, surface, and impurities while homogeneous nucleation is not affected by impurities or external surface.[23] In the reference sample, the nucleation process of perovskite crystallization on the mesoporous TiO_2 underlayer was mainly heterogeneous, which led to small crystal grains and formation of a white layer at the bottom of the film near the mesoporous TiO_2 layer (as presented in the next section). We think that the incorporation of 4M-PEACl promoted homogeneous nucleation and therefore led to larger perovskite crystal grains. In addition, bright features were observed on the $x = 0.02$ perovskite film and mainly located at perovskite crystal grain boundaries. More bright features were observed on the $x = 0.05$ perovskite film surface, and those features fully occupied the grain boundaries. Using energy-dispersive X-ray spectroscopy (EDS), we determined that those bright features have significantly higher concentration of N and lower concentration of Pb and I compared to the interior

---

T. Tran-Phu, T. Lu, Y. Liu
Research School of Chemistry
The Australian National University
Canberra 2601, Australia

J. Zheng, A. H. Baillie
The University of Sydney Nano Institute (Sydney Nano) and School of Physics
The University of Sydney
Sydney 2006, Australia

J. Zheng, A. H. Baillie
Australian Centre for Advanced Photovoltaics (ACAP)
School of Photovoltaic and Renewable Energy Engineering
University of New South Wales
Sydney 2052, Australia

U. W. Paetzold, U. Lemmer
Institute of Microstructure Technology
Karlsruhe Institute of Technology
Hermann-von-Helmholtz-Platz 1, Eggenstein-Leopoldshafen 76344, Karlsruhe, Germany

© 2023 The Authors. Advanced Energy Materials published by Wiley-VCH GmbH

16146840, 0, Downloaded from https://onlinelibrary.wiley.com/doi/10.1002/aenm.202203607 by Karlsruher Inst F. Technologie, Wiley Online Library on [27/01/2023]. See the Terms and Conditions (https://onlinelibrary.wiley.com/terms-and-conditions) on Wiley Online Library for rules of use; OA articles are governed by the applicable Creative Commons License

16146840, 0, Downloaded from https://onlinelibrary.wiley.com/doi/10.1002/aenm.202203607 by Karlsruher Inst F. Technologie, Wiley Online Library on [27/01/2023]. See the Terms and Conditions (https://onlinelibrary.wiley.com/terms-and-conditions) on Wiley Online Library for rules of use; OA articles are governed by the applicable Creative Commons License

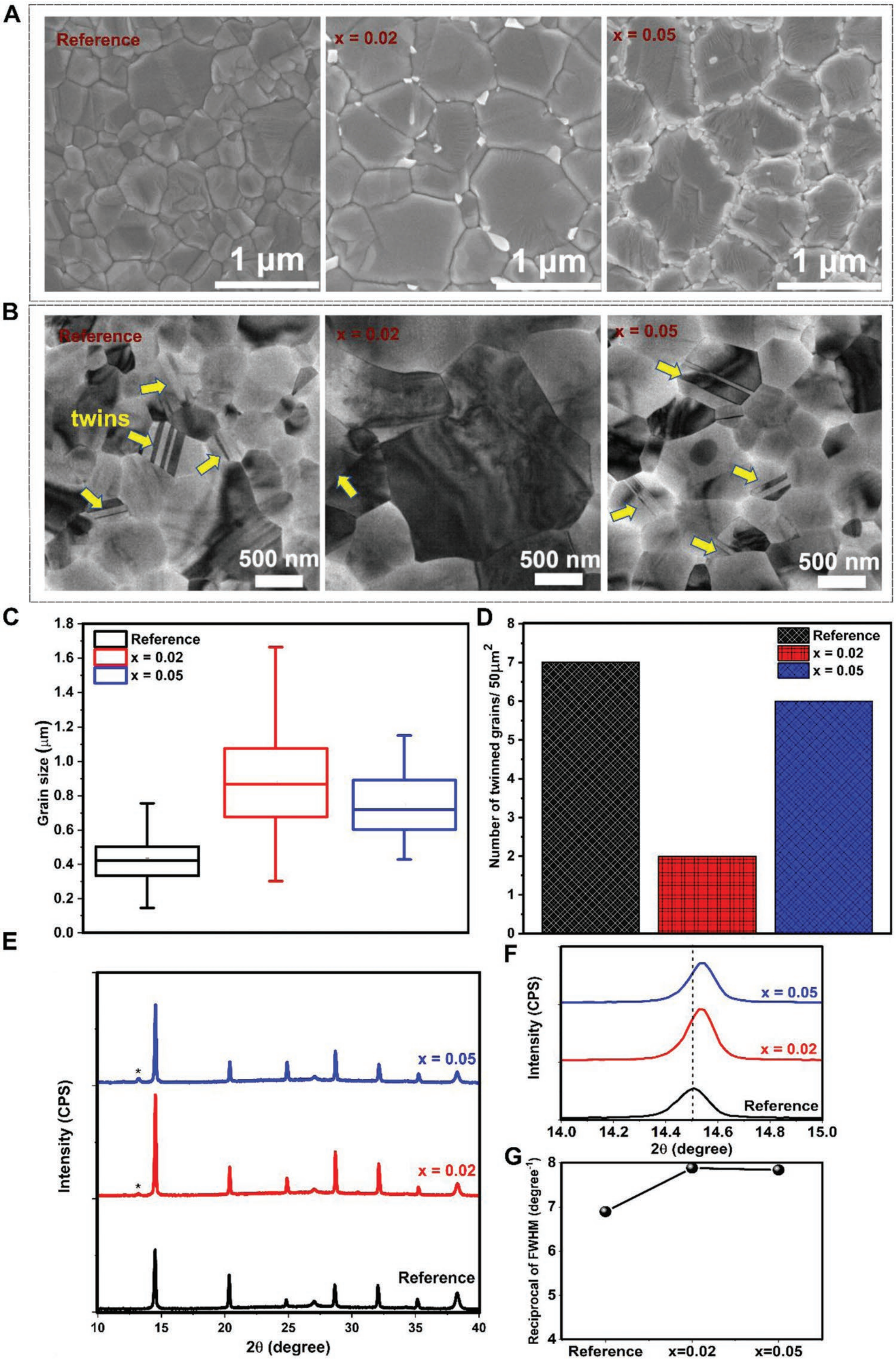

Figure 1. A) Scanning electron microscopy (SEM) images showing surface morphology of perovskite films including reference, $x = 0.02$ and $x = 0.05$ 4-methylphenethylammonium chloride. B) Bright field transmission electron microscopy (BF-TEM) of the perovskite films. C) Analysis of crystal grain sizes of the perovskite films. The arrows show the location of twinned crystal gains on the perovskite films. D) Analysis of the number of twinned crystal grains representing defects on the perovskite films. E) X-ray diffraction patterns (XRD) of the perovskite films. The * symbols show the formation of the new phases of quasi-2D perovskites. F) Magnified XRD spectra at the main peak of perovskites. G) Analysis of the reciprocal of full width at half maximum (FWHM) of the main perovskite peak of the perovskite films.

grain (Note S1, Supporting Information), which indicated that those new perovskite phases likely contained 4M-PEACl. We noted that no Cl signal was detected at the grain interior of the perovskite films according to the EDS results. Although this

© 2023 The Authors. Advanced Energy Materials published by Wiley-VCH GmbH

point spectrum EDS measurement only covered a small area of the film, the result indicated that the amount of Cl was very small at the grain interior even when the perovskite composition contained 10% of CsCl. This phenomenon was due to the volatile nature of FACl as previous reports showed that FACl sublimed during the high temperature annealing process.[24] Atomic force microscopy (AFM) measurements show that all three perovskite films have similar surface roughness average (RA), ranging from 18.8 to 23.6 nm (Figure S1, Supporting Information). AFM phase images show high contrast phase signal regions at the grain boundaries of the 4M-PEACl incorporated perovskite films (Figure S2, Supporting Information), which indicate the formation of new phases. Figure 1B shows the low magnification bright-field TEM images of the perovskite films. The microstructure and morphology of perovskite films in the TEM images were consistent with the SEM results. Additionally, the perovskite films exhibited parallel striped contrasts (highlighted with yellow pointers) on many grains, which correspond to {111} cubic twin defects.[25] The density of twin defects was obtained by counting the number of twinned grains per area of 50 μm^2 using various TEM images and the graph of the density of twin defects versus 4M-PEACl concentrations is shown in Figure 1D. The results clearly show that the $x = 0.02$ perovskite film had the lowest number of twinned grains compared to the reference film and $x = 0.05$ film. A previous report has shown that in mixed-cation (FA/Cs) perovskites, there were I-rich and Cs-rich secondary phases at the grain boundaries of perovskite crystals, which also led to the formation twin grains (defects) in the perovskite bulk.[26] We speculate that 4M-PEACl might react with the rich phases and reduce the number of defects (twin grains) in the target perovskite. A previous report has shown an empirical correlation between the electronic quality of perovskite films and the density of twin defects.[27] This indicated that $x = 0.02$ perovskite film had better electronic quality compared to the $x = 0.05$ and reference perovskite films. The impact of 4M-PEACl incorporation on the microstructure and crystal structure of the 3D perovskite films was further studied using TEM and selected area electron diffraction (SAED) analysis. Figure S3, Supporting Information, shows the bright-field TEM images and SAED patterns of the control, $x = 0.02$, and $x = 0.05$ perovskite films along two different orientations: [001] and [111]. The SAED pattern results demonstrate that all the samples had a cubic supercell structure with a $\mathrm{Im}\overline{3}$ space group. X-ray diffraction (XRD) was used to study the crystallinity and phase formation of perovskite films. As shown in Figure 1E, the reference film showed the dominant diffraction peak at $2\theta = 14.51°$ corresponding to the characteristic (001) crystal plane of the black α-FAPbI$_3$ perovskite phase. No yellow δ-FAPbI$_3$ phase at 11.6° was observed. In addition, the $x = 0.02$ and $x = 0.05$ perovskite films displayed the main diffraction peak of (001) at slightly higher angle of $2\theta = 14.54°$, indicating a small reduction in the lattice constant of the 3D perovskite crystals from 6.097 to 6.085 Å according to Bragg's law (Figure 1F). This change together with the TEM results above confirmed that 4M-PEA$^+$ cation was not incorporated into the perovskite lattice, since the large ionic radius of 4M-PEA$^+$ would otherwise increase the lattice constant. This is because the ionic radius of 4M-PEA$^+$ is much larger than FA$^+$ and Cs$^+$ and is in agreement with previous reports using other large organic cations such as phenethylammonium (PEA$^+$),[28] *n*-butylammonium (BA$^+$),[29] and 1-naphthylmethylamine (NMA$^+$).[30] The 4M-PEA$^+$ rather assembled at the grain boundaries of perovskite crystals as shown in the SEM images. The reduction in the lattice constant of perovskite could be due to changes in the lattice strain as suggested in previous reports,[29,31] potentially originating from the formation of the white features at the grain boundaries of perovskites. However, this requires further investigation, and is beyond the scope of this work. Additionally, the 4M-PEACl perovskite films exhibited a new peak at a lower angle $2\theta = 13.18°$, indicating the formation of new phases with larger *d*-spacing than the 3D perovskites. The new diffraction peak coincided with the appearance of the white features observed in the SEM images. Therefore, we assigned the new diffraction peak to these white features. Our previous report and others have shown the presence of quasi-2D perovskite $(BA)_2A_{n-1}Pb_n(I_xBr_{1-x})_{3n+1}$ when BA$^+$ was added into the 3D perovskite precursor, forming plate-like bright features on the perovskite surface.[29,32] In this case, the evidence suggests that the white features are quasi-2D perovskite composed of $(4M\text{-}PEA)_2(FA_xCs_{1-x})_{n-1}Pb_n(I_yCl_{1-y})_{3n+1}$. It is highly possible that the new phases are a mixture of different *n*-values, that is, $n = 1$ and $n = 2$. Since the polycrystalline 3D perovskites have substantial defects at the grain boundaries acting as charge-recombination centers,[33] the formation of the quasi-2D perovskites could passivate those defects and improve the internal charge carrier inside the perovskites as demonstrated by several reports.[28,29,31,34] In addition to the change in the lattice constant and formation of new phases, XRD also confirmed that the crystallinity of perovskite films was greatly enhanced upon the doping with 4M-PEACl, as indicated by the significant increase in the main peak intensity and the increase in the reciprocal full width at half maximum extracted from the XRD spectra (Figure 1G).

2.2. Effect of 4-Methylphenethylammonium Chloride Incorporation on the Surface Chemistry and Electronic Structure of Perovskite Films

We used X-ray photoelectron spectroscopy (XPS) to examine the changes in the surface elemental composition and chemical states on the perovskite films upon the incorporation of 4M-PEACl. As shown in **Figure 2**A–C, we detected some noticeable changes in the XPS spectra of C 1s, Cl 2p, and Cs 4d. In the C 1s spectra, two individual peaks positioned at 285.1 ± 0.15 eV (attributed to the adventitious carbon and from the C—C in the 4M-PEA$^+$) and 288.6 ± 0.15 eV (attributed to N—C=N in the FA$^+$) could be clearly identified. Upon the incorporation of 4M-PEACl, the intensity of the peak at 285.1 ± 0.15 eV increased while the intensity of the peak at 288.6 ± 0.15 eV decreased. The decrease in the FA$^+$ and increase in the 4M-PEA$^+$ XPS intensity upon the incorporation of 4M-PEACl indicated the presence of 4M-PEA$^+$ on the surface of the perovskite films through the formation of the quasi-2D perovskite composed of $(4M\text{-}PEA)_2(FA_xCs_{1-x})_{n-1}Pb_n(I_yCl_{1-y})_{3n+1}$ at the grain boundaries of perovskite crystals as evidenced in the SEM and XRD results. The intensity of Cl 2p positioned at 198.6 ± 0.15 eV also increased significantly upon

© 2023 The Authors. Advanced Energy Materials published by Wiley-VCH GmbH

16146840, 0, Downloaded from https://onlinelibrary.wiley.com/doi/10.1002/aenm.202203607 by Karlsruher Inst F. Technologie, Wiley Online Library on [27/01/2023]. See the Terms and Conditions (https://onlinelibrary.wiley.com/terms-and-conditions) on Wiley Online Library for rules of use; OA articles are governed by the applicable Creative Commons License

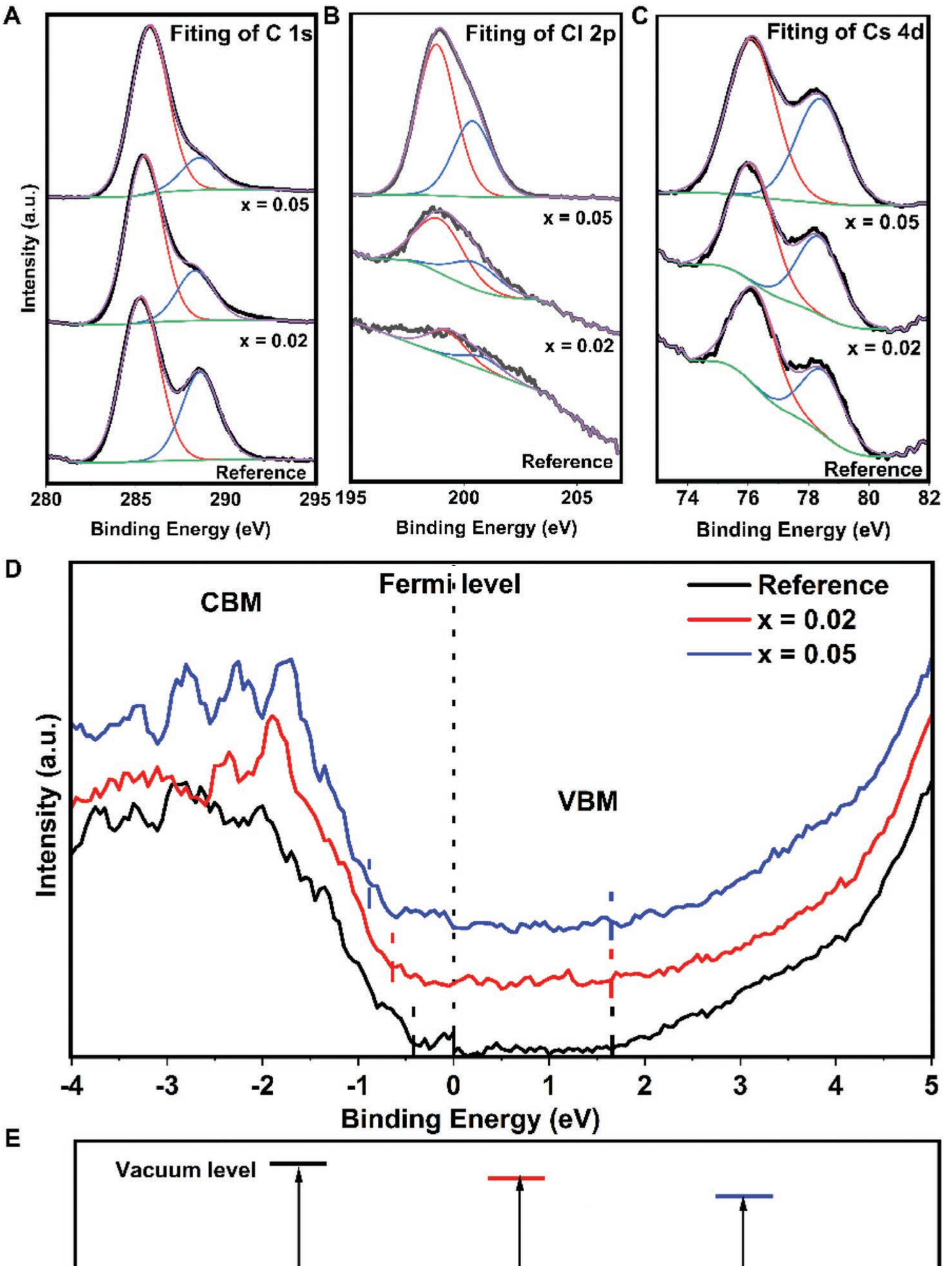

Figure 2. A) X-ray photoelectron spectroscopy (XPS) spectra of C 1s, B) Cl 2p, and C) Cs 4d of perovskite films with different concentrations of 4M-PEACl. D) Ultraviolet photoelectron spectroscopy (UPS) and inverse photoemission spectroscopy (IPES) spectra of the perovskite samples. E) Extracted values of work function, conduction band, and valence band levels of different perovskite films.

© 2023 The Authors. Advanced Energy Materials published by Wiley-VCH GmbH

16146840, 0, Downloaded from https://onlinelibrary.wiley.com/doi/10.1002/aenm.202203607 by Karlsruher Inst F. Technologie, Wiley Online Library on [27/01/2023]. See the Terms and Conditions (https://onlinelibrary.wiley.com/terms-and-conditions) on Wiley Online Library for rules of use; OA articles are governed by the applicable Creative Commons License

16146840, 0, Downloaded from https://onlinelibrary.wiley.com/doi/10.1002/aenm.202203607 by Karlsruher Inst F. Technologie, Wiley Online Library on [27/01/2023]. See the Terms and Conditions (https://onlinelibrary.wiley.com/terms-and-conditions) on Wiley Online Library for rules of use; OA articles are governed by the applicable Creative Commons License

the incorporation of 4M-PEACl. We noted that Cl signal was detected in the XPS results since the XPS measurement covered a much larger area than the point spectrum EDS measurement as presented above. Interestingly, we also detected a large enhancement in the intensity of Cs 4d (peak at 75.7 ± 0.15 eV) in $x = 0.05$ sample. We speculate that upon the addition of 4M-PEACl, more Cl^- accumulated on the surface of perovskite films and that might attract more Cs^+ especially on the $x = 0.05$ perovskite film surface. In addition, we detected significant changes in the peak positions of Cl 2p and C 1s toward lower binding energies (Table S1, Supporting Information). This indicated the decrease in oxidation states of Cl 2p and C 1s upon the incorporation of 4M-PEACl. No metallic lead (peak at 137 ± 0.15 eV) was detected in all three samples and the intensity of Pb 4f (peak at 138.3 ± 0.15 eV) slightly decreased with the addition of 4M-PEACl (Figure S4, Supporting Information). The calculated peak intensities percentage of different elements observed in the samples with the errors are presented in Table S2, Supporting Information. To understand more about the energetics of the perovskite surface, we performed ultraviolet photoelectron spectroscopy (UPS) and inverse photoemission spectroscopy (IPES) measurements on perovskite films with different concentrations of 4M-PEACl. The full UPS and IPES spectra of all perovskite films are presented in Figure 2D and the extracted values of work function (WF, the distance between the vacuum level and Fermi level), conduction band (CB) and valence band (VB) with respect to the Fermi level are presented in Figure 2E. The first key observation in the changes of the electronic structure of the perovskite films was the reduction of WF from 3.99 ± 0.1 eV in the reference film to 3.79 ± 0.1 eV in the $x = 0.02$ and 3.55 ± 0.1 eV in the $x = 0.05$ perovskite films. Since the Fermi level aligns due to the equilibrium of electrons at the perovskite/hole transport layer (HTL) interface in perovskite solar cells, we hypothesize that this reduction in the WF of perovskite caused more upward energy band bending at the interface due to the increasing difference between the WF, which would lead to more efficient hole extraction in the devices. In addition, the reference perovskite film was n-type with the CB positioned 0.42 ± 0.1 eV above and the VB positioned 1.7 ± 0.2 eV below the Fermi level. Upon the incorporation of 4M-PEACl, the CB moved upward while the VB was unchanged regarding the Fermi level. Additionally, we observed a decrease in the density of states close to the valence band cut-off in all three samples. We note that the energy gaps energy gap in the reference, $x = 0.02$ and $x = 0.05$ perovskite samples were 2.12 ± 0.2 eV, 2.34 ± 0.3 eV, and 2.58 ± 0.3 eV, respectively. All the energy gaps are substantially higher than the optical bandgaps expected from these perovskite compositions. This phenomenon can come from two reasons: 1) The difference between the principles of the two measurement techniques, that is, the optical gap is based on excited states while the energy gap is based on ionized states[35] and 2) bandgap widening at the surface of the materials.[36] The energy alignments between the perovskite and the Spiro-MeOTAD are illustrated in Figure S5, Supporting Information. The XPS and UPES/IPES results clearly showed that the incorporation of 4M-PEACl into the perovskite precursor significantly modified the surface chemistry and electronic structure of perovskite films.

2.3. Impact of 4-Methylphenethylammonium Chloride Incorporation on the Optoelectronic Properties of Perovskites

We investigated the optical properties of perovskite films using ultraviolet-visible (UV–vis) absorption spectra and photoluminescence (PL). **Figure 3**A shows the slight blue shift in the absorption onset of the 4M-PEACl incorporated perovskite films. In agreement with the UV–vis results, the main emission peak of the PL spectra slightly shifted from ≈800 nm in the reference sample to ≈797 nm in the 4M-PEACl incorporated samples, corresponding to an optical bandgap of ≈1.55 eV for the perovskite films. The Tauc plot presented in Figure S6, Supporting Information, further confirmed the values of the optical bandgaps. Time-resolved PL measurements show the enhancement in carrier lifetime of $x = 0.02$ perovskite film as compared to the reference sample. However, the lifetime slightly decreased when the molar ratio of 4M-PEACl increased to 5% (Figure 3B). We also performed PL imaging of perovskite solar cells using the perovskite films as active layers (details will be shown in the next section). As shown in Figure 3C, the average PL intensity was significantly enhanced in the 4M-PEACl incorporated devices, especially at the 4M-PEACl concentration of $x = 0.02$. In addition, the reference device showed significant inhomogeneity on the PL signal, while the PL intensity was relatively uniform on the $x = 0.02$ and $x = 0.05$ devices. The inhomogeneity in the PL signal of the reference film came from a $(FA_xCs_{1-x})_2Pb_3(I_yCl_{1-y})_8(DMSO)_2$ intermediate phase at the bottom of the perovskite films near the ms-TiO_2 electron transport layer (ETL), as discussed later.

2.4. Photovoltaic Performance

To understand the effect of 4M-PEACl incorporation on the solar cell performance, we employed the normal n-i-p perovskite cell structure with glass/fluorine doped tin oxide (FTO)/compact TiO_2/mesoporous TiO_2/perovskite/Spiro-MeOTAD/Au. **Figure 4**A shows the variations in photovoltaic parameters extracted from the reverse *JV* scans of perovskite solar cells with different molar concentrations (1%, 2%, 3%, and 5%) of 4M-PEACl. At least 12 devices in each condition were fabricated. The reference devices showed an average reverse scan efficiency of 19.6 ± 1.6% with high variation in the open circuit voltage (V_{OC}) and fill factor (FF). The device performance was significantly enhanced upon the incorporation of 4M-PEACl, reaching the highest values (average PCE of 23.9 ± 0.3%, reverse scan) at the optimal concentration of $x = 0.02$ mol ratio of 4M-PEACl. The device performance was slightly lower at higher mol ratios of 4M-PEACl, averaging at 23.6 ± 0.2% and 22.7 ± 0.3% at $x = 0.03$ and $x = 0.05$, respectively. Cross-sectional SEM images of reference, $x = 0.02$ and $x = 0.05$ perovskite solar cells were examined (Figure 4B). The perovskite active layer in the reference device displayed small crystal grains with 2–3 grains stacking on each other while the perovskite crystallinity in $x = 0.02$ and $x = 0.05$ samples was significantly enhanced and mostly a single grain covered the entire active layer thickness. In addition, the bright features were not only observed on the surface but also in the bulk (mostly at the grain boundaries) in the

© 2023 The Authors. Advanced Energy Materials published by Wiley-VCH GmbH

16146840, 0, Downloaded from https://onlinelibrary.wiley.com/doi/10.1002/aenm.202203607 by Karlsruher Inst F. Technologie, Wiley Online Library on [27/01/2023]. See the Terms and Conditions (https://onlinelibrary.wiley.com/terms-and-conditions) on Wiley Online Library for rules of use; OA articles are governed by the applicable Creative Commons License

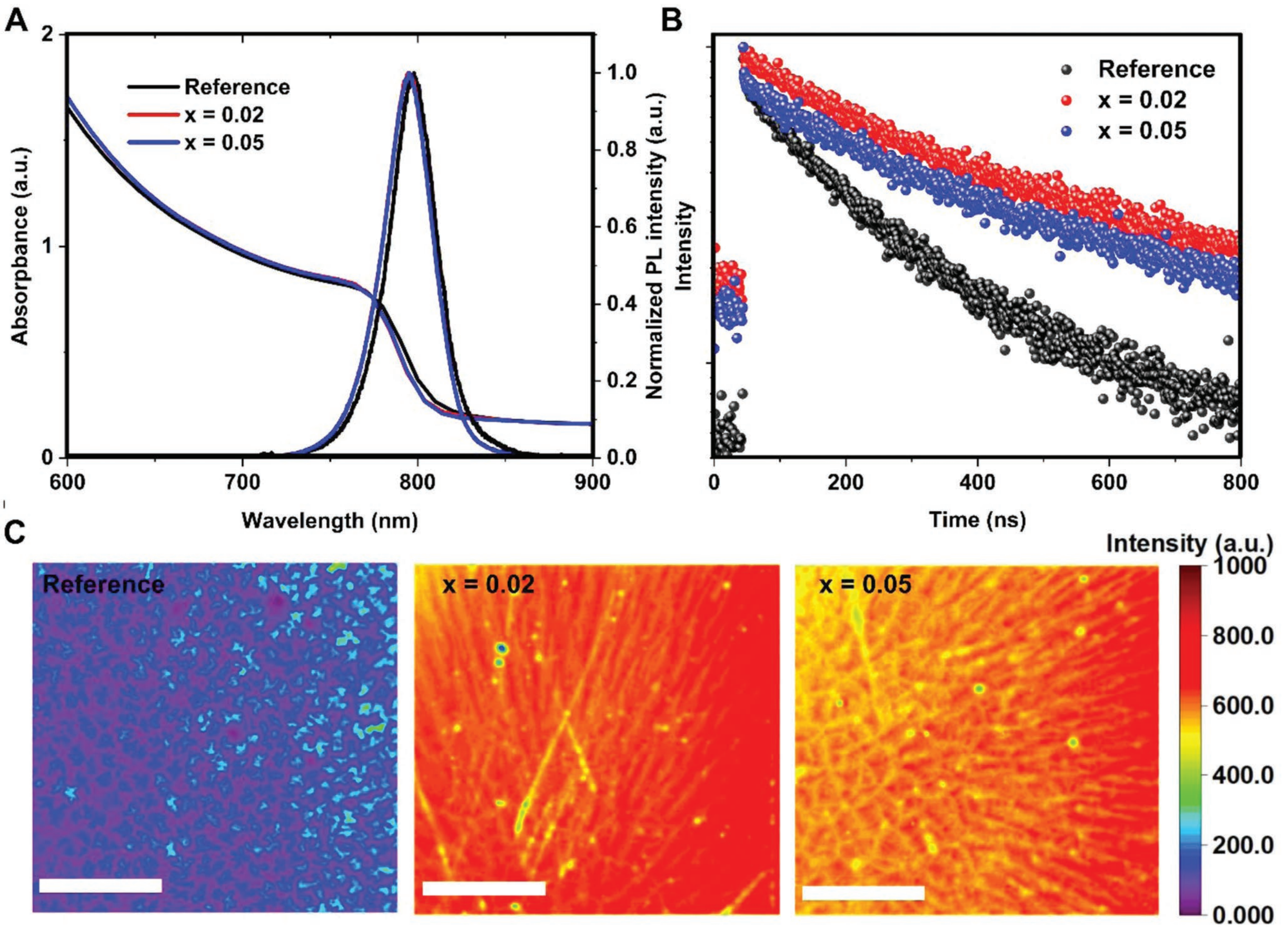

Figure 3. A) Absorption spectra and normalized photoluminescence (PL) spectra of perovskite films including reference, $x = 0.02$ and $x = 0.05$ 4-methylphenethylammonium chloride. B) Time-resolved PL of the perovskite films. The PL intensity is on a logarithmic scale. C) PL images of perovskite solar cells with different concentrations of 4M-PEACl. The scale bar is 400 µm.

$x = 0.05$ perovskite film. The current density–voltage (JV) curves in both reverse and forward scans of the champion device (condition $x = 0.02$, abbreviated as target hereafter) and the reference device are shown in Figure 4C. The champion target device displayed an efficiency of 24.2% (reverse scan)/23.0% (forward scan) and a steady state performance of 23.7% (Figure S7, Supporting Information). This value is one of the highest efficiencies for MA-free perovskite solar cells (Table S3, Supporting Information). In addition, the hysteresis was greatly suppressed in the target device. Our data indicates that the improved perovskite crystallinity and the changes in the electronic structure as demonstrated above (especially the reduction in WF) of perovskites upon the addition of 4M-PEACl were responsible for the performance enhancement of the solar cells. External quantum efficiency (EQE) of reference and target devices, along with the integrated short circuit current density (J_{SC}) are displayed in Figure 4D. The integrated short circuit current density of the target device was 24.5 mA cm^{-2}, which was 2.5% smaller than the J_{SC} obtained the from JV curve (25.1 mA cm^{-2}) and within the acceptable deviation range in perovskite solar cells. The EQE of the target device was significantly higher than the reference device, especially in the 400–600 nm wavelength region. A white perovskite layer was observed from the glass side of the reference device while the target device was completely black (Figure S8A, Supporting Information). The white layer was responsible for the inhomogeneity of the PL signal of the reference device. This was located at the bottom of the perovskite active layer (in contact with the ETL layer), therefore it was not detected by previous characterization techniques (SEM, TEM, XRD). We performed time-of-flight secondary ion mass spectrometry (ToF-SIMS) of complete perovskite cells to understand the profile of different elements in the devices. The device structure can be represented by the ToF-SIMS profiles of Au$^-$, CN$^-$, PbI$^-$, TiO$^-$, and SnO$_2^-$ as shown in Figure S8B,C, Supporting Information. Interestingly, we detected higher S$^-$ near to the TiO$_2$ interface in the reference sample compared to the target device. Since the main source of S$^-$ is the dimethyl sulfide (DMSO, C$_2$H$_6$SO) solvent used for preparing the perovskite precursor, the white perovskite layer was most likely a $(FA_xCs_{1-x})_2Pb_3(I_yCl_{1-y})_8(DMSO)_2$ intermediate phase formed during the crystallization and remained trapped in the reference perovskite film. Upon the addition of 4M-PEACl,

© 2023 The Authors. Advanced Energy Materials published by Wiley-VCH GmbH

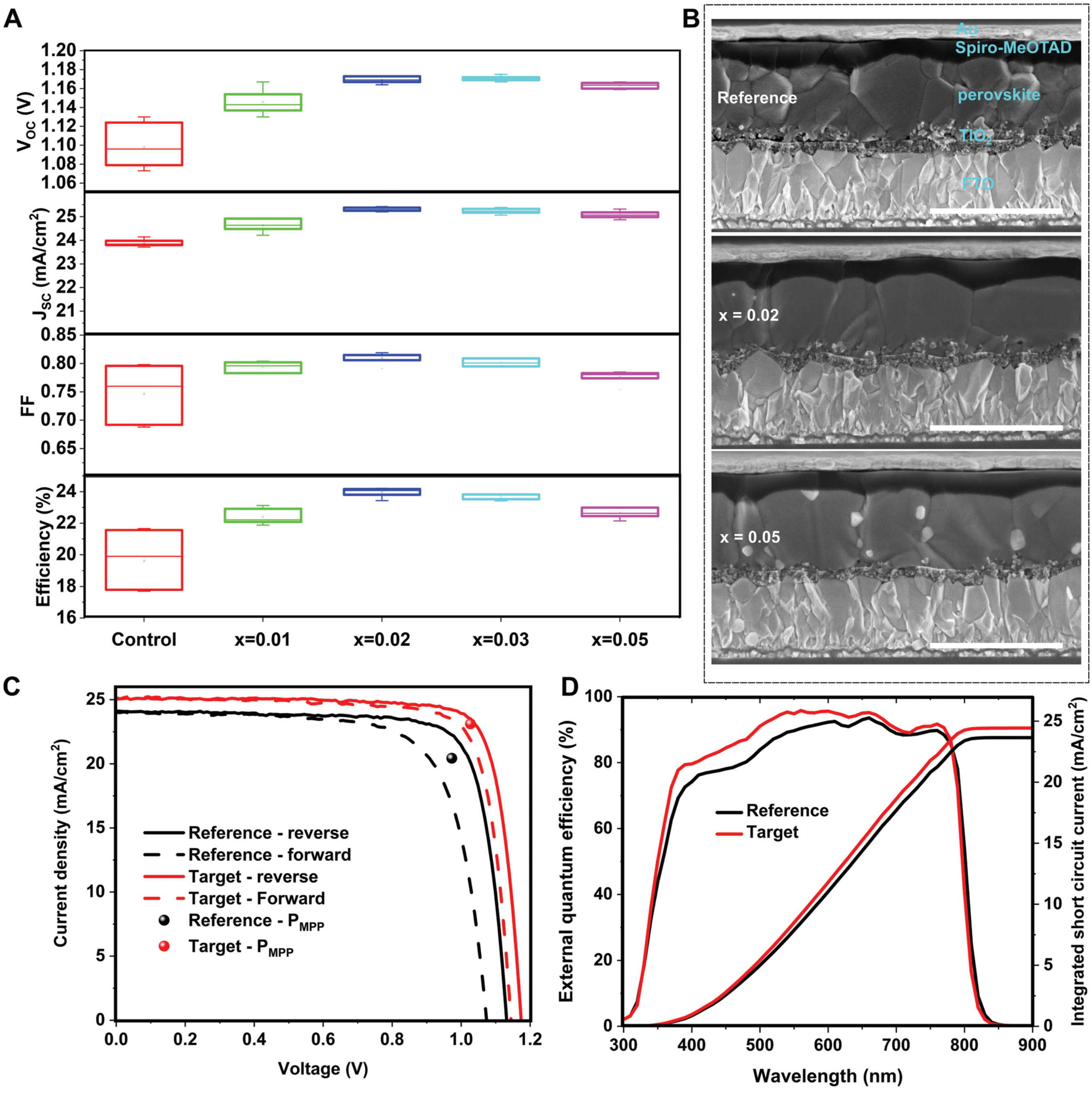

Figure 4. A) Photovoltaic parameters (open circuit voltage V_{OC}, short circuit current density J_{SC}, fill-factor (FF) and efficiency of perovskite solar cells employing different perovskites. The photovoltaic parameters were extracted from reverse current–voltage scans with a scan rate of 50 mVs^{-1}. 12 devices were fabricated in each condition in the same batch. B) Cross-sectional scanning electron microscopy (SEM) of perovskite solar cells. The scale bar is 1 µm. C) Current density–voltage (*JV*) curves of reference and target ($x = 0.02$) perovskite solar cells. D) External quantum efficiency (EQE) spectra of perovskite solar cells.

the crystallization of perovskite was greatly enhanced, and the intermediate phase was fully converted to α-FAPbI$_3$ perovskite phase (Figure 1E–G). In addition, as shown in Figure S9, Supporting Information, we detected high intensity of Cl$^-$ in the 4M-PEACl incorporated samples throughout the bulk of the perovskite films. This indicated that Cl$^-$ not only accumulated on the surface of the perovskite films, but also throughout the bulk of the films.

2.5. Investigation of Defects, Recombination, and Stability of Perovskite Solar Cells upon the Incorporation of 4-Methylphenethylammonium Chloride

We performed thermally stimulated current (TSC) measurements for the reference and target perovskite solar cells to reveal shallow trap states in the perovskite absorbers.[32,37] As shown in **Figure 5**A, the control device exhibited three distinct

© 2023 The Authors. Advanced Energy Materials published by Wiley-VCH GmbH

16146840, 0, Downloaded from https://onlinelibrary.wiley.com/doi/10.1002/aenm.202203607 by Karlsruher Inst F. Technologie, Wiley Online Library on [27/01/2023]. See the Terms and Conditions (https://onlinelibrary.wiley.com/terms-and-conditions) on Wiley Online Library for rules of use; OA articles are governed by the applicable Creative Commons License

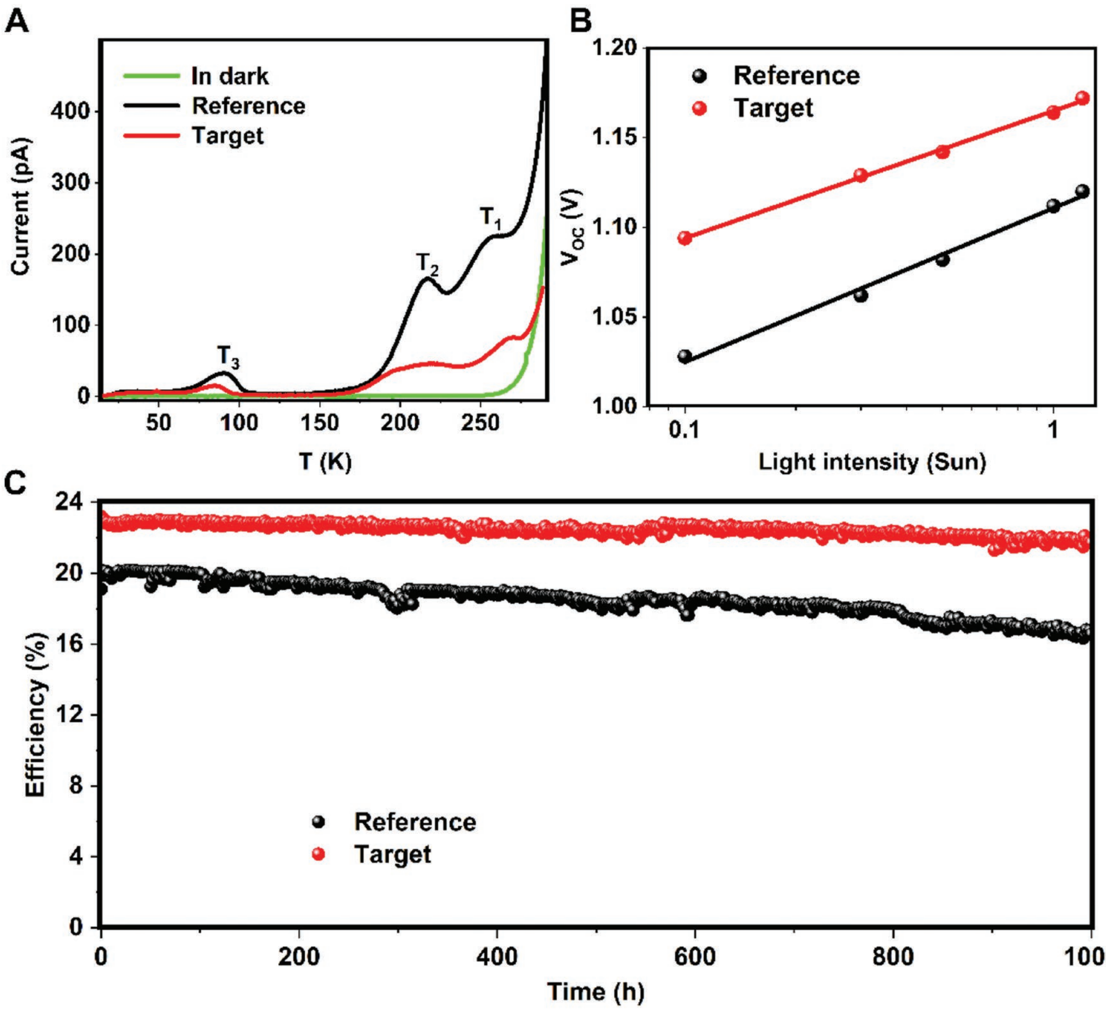

Figure 5. A) Thermally stimulated current (TSC) spectra of reference and target perovskite solar cells. B) Light intensity dependent open circuit voltage measurement of the perovskite cells. C) Light stability of reference and target perovskite solar cells. The devices were kept under light (white LED light calibrated at 1 Sun intensity), and at fixed voltages close to their maximum power points voltages. The cell temperatures were maintained at 25 °C and the devices were in a nitrogen-filled environment during the tests.

peaks around 90 K (T_1), 217 K (T_2), and 257 K (T_3). The peak at T_3 originated from the HTL Spiro-MeOTAD as in our previous report and the other two peaks at T_1 and T_2 came from the perovskite active layer.[37a] The average trap depth (E_t) of the two peaks was calculated using the formula:

$$E_t = k_B\, T \ln\left(\frac{T^4}{b}\right) \tag{1}$$

where k_B is the Boltzmann constant, T is the temperature of the TSC peak, and b is the heating rate. The current magnitude of the TSC signal (I) is a measure of the number of traps and the lower limits of trap density (N_t) was calculated using Equation (2) below:

$$\int I dt \le e N_t h A \tag{2}$$

where e is elementary charge, h is the thickness of the active layer, and A is the active area of the device.

Based on Equations (1) and (2), two trap levels at the depth of 539 and 443 meV are present in the perovskite active layer of the control devices. The total trap density in the reference device was estimated to be 2.05×10^{17} (cm^{-3}). The target device also showed three different peaks at the same temperatures as the control sample, however the peaks at T_1 and T_2 were significantly broader than for the control devices. More importantly, the current magnitudes at those two peaks were much lower than the control device. The total trap density in the perovskite active layer of the target device was estimated to be 4.84×10^{16} (cm^{-3}), which was 4 times lower than in the reference device. Light intensity dependent V_{OC} measurements were applied to extract the ideality factors (n_{id}) in the reference and target devices following procedures in previous reports (Figure 5B).[38] The ideality factor in the control device was calculated to be 1.43 while the ideality factor in the target device was 1.19. The reduction in the n_{id} indicated that the trap-assisted bulk Shockley–Read–Hall recombination in the device was mitigated by the incorporation of 4M-PEACl. These results agree well with the enhanced

© 2023 The Authors. Advanced Energy Materials published by Wiley-VCH GmbH

16146840, 0, Downloaded from https://onlinelibrary.wiley.com/doi/10.1002/aenm.202203607 by Karlsruher Inst F. Technologie, Wiley Online Library on [27/01/2023]. See the Terms and Conditions (https://onlinelibrary.wiley.com/terms-and-conditions) on Wiley Online Library for rules of use; OA articles are governed by the applicable Creative Commons License

crystallinity, reduction in twin defects, and improved device performance as demonstrated in the previous sections.

We investigated the light stability of reference and target perovskite solar cells. The unencapsulated devices were kept under light (white LED with 1 Sun intensity), biased near to the maximum power point voltages and the device temperatures were maintained at 25 °C in N_2 environment. As shown in Figure 5C, the reference device retained 82.1% of the initial performance after 1000 h as the efficiency decreased from 20.1% to 16.5%. In comparison, the target device retained 93.5% of the original performance as the efficiency was reduced from 23.2% to 21.7% after 1000 h. The result clearly showed that the light stability of perovskite solar cells was significantly improved with the incorporation of 4M-PEACl. We also tested the heat stability and ambient stability of perovskite films and perovskite solar cells. As shown in Figure S10, Supporting Information, both the reference and target perovskite films were stable, while the perovskite film with a composition of $FAPbI_3$ + 35 mol% MACl degraded significantly at 100 °C for 120 h. At the device level, the device with $FAPbI_3$ + 35% MACl perovskite composition retained ≈86% of the initial performance after 120 h at 100 °C. In comparison, the reference and target devices retained ≈94% and 97% of their original performance, respectively. Our results clearly show that the MA-free perovskites have better thermal stability than the MA-containing perovskites, however the target perovskite with 4M-PEACl only showed marginal improved thermal stability compared to the reference perovskite without 4M-PEACl. In terms of ambient stability, we exposed the unencapsulated reference and target films and solar cells in a humid environment of 85% relative humidity (RH) to accelerate the degradation. As shown in Figure S11, Supporting Information, the reference perovskite film degraded significantly after 120 h at 85% RH as evidenced by the reduction in the absorbance as well as the emergence of a new peak at ≈450 nm (PbI_2). In contrast, the target perovskite film showed much enhanced ambient stability compared to the reference film as the absorbance spectra only slightly changed. The results were consistent with the finding that quasi-2D perovskites at the grain boundaries could greatly reduce possible ingression pathway of moisture through the grain boundaries of 3D perovskites.[28,31] At the device level, the target perovskite solar cell also showed significantly enhanced ambient stability compared to the reference perovskite cell. The reference and target perovskite solar cells retained ≈65% and 86% of their initial performance after 120 h at 85% RH, respectively. The results clearly show that the perovskite samples were more susceptible to ambient (moisture) than to light and/or heat exposure. The ambient stability of perovskite solar cells is significantly enhanced with proper encapsulation as demonstrated in the next section.

2.6. Performance and Stability of Four-Terminal Perovskite-Silicon Tandem Solar Cells

Finally, we utilized this low-moderate perovskite composition in 4-terminal perovskite-silicon tandem solar cells. Without the current matching requirement in the 4-terminal tandem configuration, this low-moderate bandgap perovskite top cell can deliver close to the optimal efficiency while potentially offering much greater operational stability compared to high bandgap perovskites with mixed-halide compositions.[39] Semi-transparent perovskite solar cells were fabricated using the structure glass/indium tin oxide (ITO)/SnO_2/perovskite/Spiro-MeOTAD/MoO_3/indium zinc oxide (IZO)/Au fingers. It is worth noting that SnO_2 with a low processing temperature (150 °C) was used as the ETL instead of the high processing temperature TiO_2 (500 °C) since the ITO substrate used in the semi-transparent cell is only stable up to 300 °C. This led to higher FF but slightly lower V_{OC} compared to the TiO_2-based devices as shown in Figure S12, Supporting Information. A schematic of the 4-terminal mechanically stacked perovskite-silicon tandem solar cells is illustrated in **Figure 6**A and the cross-sectional SEM image of a semi-transparent perovskite solar cell is shown in Figure 6B. The performance of each sub-cell is presented in Figure 6C and summarized in **Table 1**. The champion semi-transparent perovskite top cell showed an efficiency of 22.9% in reverse scan, 22.2% in forward scan and a steady state efficiency of 22.6%. Importantly, the semi-transparent perovskite cells displayed a high transparency of up to 80% in the infrared (Figure S13, Supporting Information). Under a semi-transparent perovskite cell filter, which had all the layers similar to the active semi-transparent perovskite cells, a bottom passivated emitter, rear locally-diffused (PERL) silicon cell with an original efficiency of 23.8% retained an efficiency of 7.7%. The structure of the silicon solar cell is illustrated in Figure S14, Supporting Information. The EQE spectrum of the silicon cell, semi-transparent perovskite cell and silicon cell under perovskite filter are presented in Figure 6D. Overall, the EQE results were in excellent agreement with the JV results of the devices. The integrated J_{SC} of the semi-transparent perovskite top cell was 23.6 mA cm^{-2}, which was 2% lower than the J_{SC} extracted from the JV curves of the device. On the other hand, the integrated J_{SC} of the silicon cell performing alone and under semi-transparent perovskite were 41.7 mA cm^{-2} and 13.7 mA cm^{-2}, respectively, in both the JV and EQE results. Overall, the efficiency of 4-terminal perovskite-silicon tandem solar cell was calculated to be 30.3%, which is one of the highest values reported for this type of tandem devices using the perovskite top cells with comparable active areas.[32,40] We also fabricated a 1 cm^2 semi-transparent perovskite top cell and combined with a 1 cm^2 silicon bottom cell in a 1 cm^2 size-matched tandem cell. The performance of the size-matched 4-terminal perovskite-silicon tandem is shown in Figure S15, Supporting Information, and summarized in Table S4, Supporting Information. A picture of a semi-transparent perovskite cells is shown in Figure 6E. The champion 1 cm^2 semi-transparent perovskite cell exhibited an efficiency of 21.7% (reverse scan)/20.7% (forward scan) and a steady state efficiency of 21.3%. The 1 cm^2 silicon bottom cell with a stand-alone initial efficiency of 21.7% retained an efficiency of 7.1% when operating under the 1 cm^2 semi-transparent perovskite top cell. Overall, the 1 cm^2 4-terminal perovskite-silicon tandem showed an efficiency of 28.4%. The efficiency in this 1 cm^2 size matching tandem solar cell was significantly lower than the efficiency obtained from the previous measurement using filter technique, mostly due to the efficiency of the perovskite top cells. This highlights the need to overcome challenges in scaling up perovskite solar cells.[41] In addition, the bottom silicon cell with a moderate efficiency

© 2023 The Authors. Advanced Energy Materials published by Wiley-VCH GmbH

16146840, 0, Downloaded from https://onlinelibrary.wiley.com/doi/10.1002/aenm.202203607 by Karlsruher Inst F. Technologie, Wiley Online Library on [27/01/2023]. See the Terms and Conditions (https://onlinelibrary.wiley.com/terms-and-conditions) on Wiley Online Library for rules of use; OA articles are governed by the applicable Creative Commons License

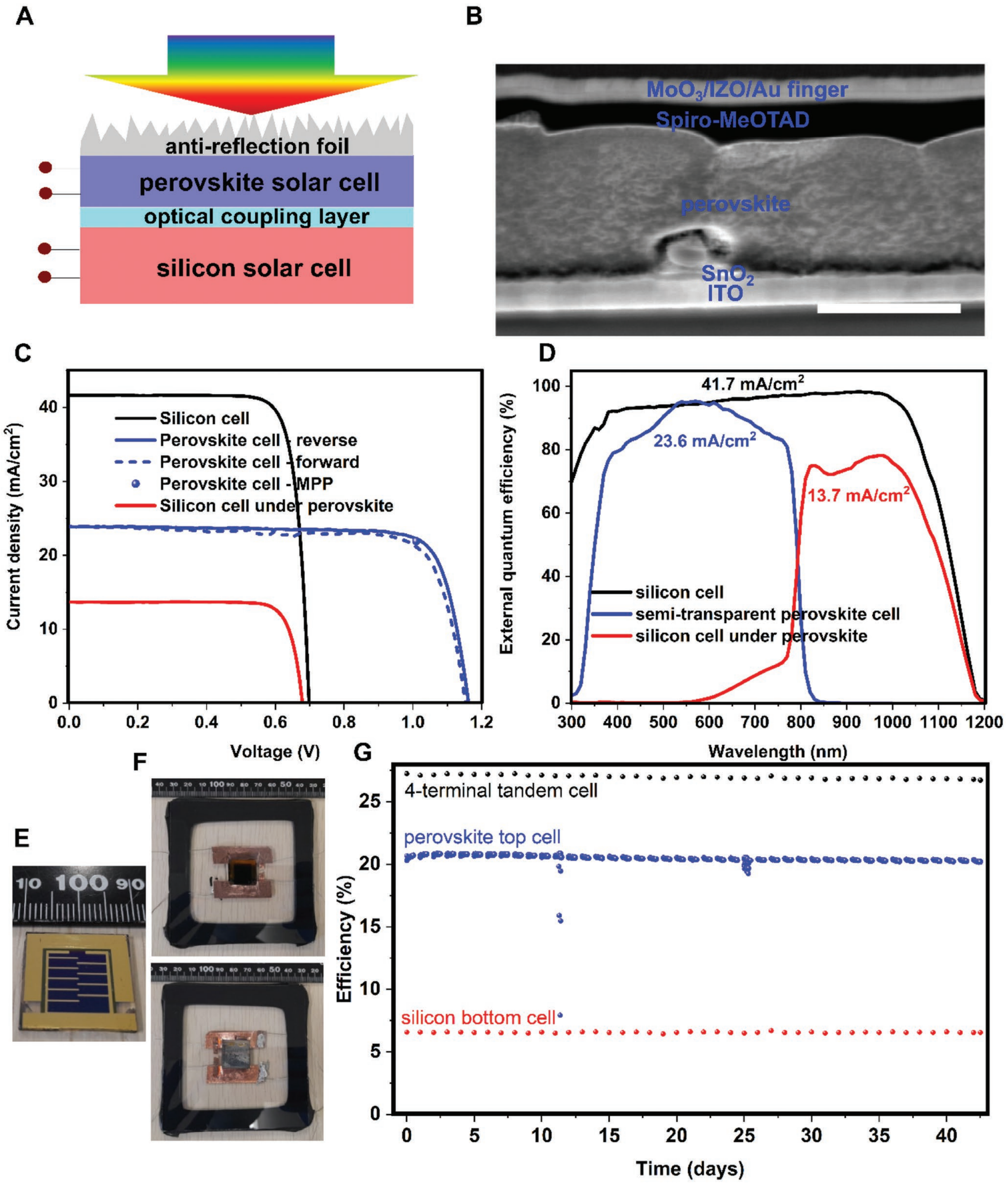

Figure 6. A) Schematic of 4-terminal perovskite-silicon tandem solar cells. B) Cross-sectional SEM images of a semi-transparent perovskite solar cell with a structure glass/ITO/SnO_2/perovskite/spiro-MeOTAD/MoO_3/IZO/Au finger. The scale bar is 500 nm. C) *JV* curves of the sub-devices in the tandem configuration. D) EQE of the sub-devices in the tandem configuration. E) Picture of a 1 cm^2 semi-transparent perovskite solar cell. F) Pictures of an encapsulated 4-terminal perovskite-silicon tandem solar cell from top and bottom. G) Operational stability the encapsulated 4-terminal perovskite-silicon tandem solar cell for 42 day/night cycles.

© 2023 The Authors. Advanced Energy Materials published by Wiley-VCH GmbH

16146840, 0, Downloaded from https://onlinelibrary.wiley.com/doi/10.1002/aenm.202203607 by Karlsruher Inst F. Technologie, Wiley Online Library on [27/01/2023]. See the Terms and Conditions (https://onlinelibrary.wiley.com/terms-and-conditions) on Wiley Online Library for rules of use; OA articles are governed by the applicable Creative Commons License

Table 1. Photovoltaic parameters of perovskite silicon tandem solar cells.

	Area [cm^2]	V_{oc} [V]	J_{sc} [mA cm^{-2}]	FF	PCE [%]
Silicon cell	4	0.698	41.7	0.819	23.8
Semi-transparent perovskite cell—Reverse	0.25	1.131	24.0	0.842	22.9
Semi-transparent perovskite cell—Forward		1.122	24.0	0.824	22.2
Semi-transparent perovskite cell—MPP					22.6
Silicon cell under perovskite filter	4	0.678	13.7	0.825	7.7
Tandem efficiency					30.3

of 21.7% was comparable with the efficiency of commercial silicon solar modules, which would be used for large area perovskite-silicon tandem solar modules. Therefore, the efficiency of 28.4% in this work would be expected in practical perovskite-silicon tandem solar modules. The tandem devices were encapsulated using polyisobutylene edge-seal method and the picture of the encapsulated cell can be seen in the inset of Figure 6F.[42] The operational stability of the tandem device was examined by exposing the device under day/night cycles. The temperature of the devices was between 10 and 60 °C during the test. The efficiency of the perovskite top cell was measured continuously while the efficiency of the silicon bottom cell was checked periodically. The performance of the encapsulated device was lower than the non-encapsulated device due to the presence of the top cover encapsulating glass. After 42 day/night cycles in ambient, the tandem device showed excellent operational stability, retaining over 98% of the initial performance (reduced from 27.2% to 26.7%). Very few reports demonstrated the operational stability of 4-terminal perovskite-silicon tandem solar cells. Coletti et al. tested bifacial perovskite-silicon tandem modules for 100 h under continuous light; however, the stability of the devices was not reported.[43] In the most recent report, Yu et al. performed light stability of stand-alone semi-transparent perovskite solar cells and showed that the device retained 90% of the initial efficiency after 500 h.[40c] We believe the results presented here demonstrate the state-of-the-art operational stability of 4-terminal perovskite-silicon tandem solar cells, further affirming the benefit of using low-moderate bandgap perovskite compositions for tandem applications.

3. Conclusion

In conclusion, we demonstrated a facile method to improve the bulk quality of a MA-free perovskites with low-moderate bandgap by adding 4M-PEACl into the perovskite precursor. Although 4M-PEACl was not incorporated into the 3D perovskite lattice, this approach facilitated the conversion to α-FAPbI$_3$ perovskite phase and greatly enhanced the crystallinity while suppressing the defects (e.g., twin grains) in the perovskite films. Quasi-2D perovskites formed at the grain boundaries of 3D perovskite passivated defects and improved the internal carrier transport properties of the 3D perovskites. The incorporation of 4M-PEACl also significantly changed the surface chemistry of the perovskite films and made the perovskite electronic structure more favorable for hole extraction. The result is a significant improvement in the performance and light stability of perovskite solar cells. We achieved a steady state efficiency of 23.7% (24.2% reverse scan, 23.0 forward scan) for MA-free perovskite solar cells and the device retained more than 93% of the initial performance after 1000 h operating under constant illumination. By combining with silicon solar cells in a 4-terminal mechanically stacked tandem, an efficiency of 30.3% was obtained, which is one of the highest values reported for this type of device. More importantly, the tandem devices show excellent operational performance, retaining more than 98% of their performance after 42 day/night cycles in ambient.

4. Experimental Section

Materials: Formamidinium iodide, 4M-PEACl, *n*-octylammonium bromide, and TiO$_2$ paste were ordered from GreatCell Solar Materials. Lead iodide was ordered from TCI Co., LTD. Spiro-MeOTAD was ordered from Lum-Tech. Refractive index matching layer (series AA, refractive index = 1.414) was ordered from SPI Supplies. Silicone was ordered from The Dow Chemical Company (SYLGARD 184 Silicone Elastomer). Tin(IV) oxide, 15% in H$_2$O colloidal dispersion was ordered from Alfa Aesar. Other materials were ordered from Sigma-Aldrich.

Perovskite Solar Cell Fabrication: FTO glass substrates were cut into 1.45 cm × 1.25 cm and cleaned in ultrasonic bath with detergent for 90 min and for 15 min in acetone, 2-propanol and ethanol sequentially. The substrates were further cleaned using UV Ozone for 30 min before being immediately transferred to a N$_2$ purging glove box. 70 nm of compact TiO$_2$ was deposited twice on the substrates by spinning a solution of titaniu(IV) isopropoxide (TTIP) in 2-propanol at 5000 rpm for 15 s. The substrates were then annealed at 500 °C for 30 min in air. 100 nm of mesoporous TiO$_2$ was deposited on the substrates by spinning a solution of TiO$_2$ paste in ethanol at 5000 rpm for 15 s. The substrates were then annealed at 500 °C for 30 min in air. The 3D perovskite precursor was prepared by mixing 1.3 M PbI$_2$, 1.3 M of FAI, and 0.13 M CsCl in 1 mL of DMF/DMSO (4:1 volume ratio). 4M-PEACl was added into the 3D perovskite precursor with different mol concentration from 1% to 5%. Perovskite was deposited on the substrates by spinning the solution (40 µL) at 1000 rpm for 10 s (acceleration rate 200 rpm s^{-1}) and 4000 rpm (acceleration rate 1000 rpm s^{-1}) for 25 s. 5 s before the program ends, chlorobenzene (120 µL) was quickly dropped on the middle of the substrates. This was then followed by an annealing at 150 °C for 10 min and 100 °C for 10 min on a hotplate. *n*-octylammonium iodide (2 mg mL^{-1} in 2-propanol) was spun on the substrates at 5000 rpm for 30 s. The substrates were further annealed at 100 °C for 5 min. Spiro-MeOTAD layer was deposited on the perovskite films by spinning solution of Spiro-MeOTAD (40 µL, 72 mg mL^{-1}) in chlorobenzene with Li-TFSI (17.5 µL, 520 mg mL^{-1} in acetonitrile) and 4-tBp (28.5 µL) at 3500 rpm for 30 s. 100 nm of Au was deposited on the substrates by thermal evaporation through a shadow mask with an active area of 0.16 cm^2. For semi-transparent devices, indium-doped tin oxide (ITO) glass substrates were used instead of FTO substrates.

© 2023 The Authors. Advanced Energy Materials published by Wiley-VCH GmbH

16146840, 0, Downloaded from https://onlinelibrary.wiley.com/doi/10.1002/aenm.202203607 by Karlsruher Inst F. Technologie, Wiley Online Library on [27/01/2023]. See the Terms and Conditions (https://onlinelibrary.wiley.com/terms-and-conditions) on Wiley Online Library for rules of use; OA articles are governed by the applicable Creative Commons License

The SnO_x ETL was deposited by diluting the Tin(IV) oxide colloidal dispersion in deionized (DI) water (1:3 volume ratio). The SnO_x precursor was spun on the substrates at 3000 rpm for 30 s, followed by an annealing step at 150 °C for 30 min. The perovskite and Spiro-MeOTAD HTL layers were deposited following the previous described method. 10 nm of MoO_3 was deposited on the substrate by thermal evaporation at very low vacuum ($\approx 5 \times E^{-7}$ Torr). 30 nm of IZO was then deposited on the substrates by radio frequency sputtering through a shadow mask with an active area of 0.36 cm^2. Metal grids were deposited on top of the IZO layers by thermal evaporation. For large area device, substrates with size of 1.8 cm × 1.8 cm were used instead and a shadow mask with an aperture of 1.21 cm^2 was used to define the active area. To integrate large area perovskite solar cell and silicon solar cell in an area-matched four-terminal tandem, the 1 cm^2 PERL silicon cell was directly placed underneath the semi-transparent perovskite top cell. A refractive index matching layer was put between the two cell and a textured foil was placed on top of the perovskite top cell. Each cell was measured independently under simulated AM1.5G light. Four-terminal perovskite-silicon tandem solar cells were encapsulated between two glass substrates using butyl rubber edge sealant inside a glove box. Butyl rubber edge sealant was laid around the edge of each glass substrate while the device was attached in the middle of the glass substrate. The whole stack was placed in a custom-built jig and put on a hot plate at 95 °C. The thermal insulator in the middle of the jig limited the temperature experienced by the cell to below 70 °C. The four screws on the jig were tightened to press the stack down and the jig was kept at 95 °C for 15 min before cooling down to room temperature.

Silicon Solar Cell Fabrication: Float-zone (FZ) *n*-type 2 Ohm-cm wafers were first to a thickness of ≈280 µm in a 25% concentration tetramethylammonium hydroxide (TMAH) solution at 85 °C. A photolithography step with SiOx/SiN3N4 mask was applied to define cell regions on the rear side of the wafer for diffusion. Heavy boron diffusion was performed to get a boron emitter at the rear with a sheet resistance R_{sh} of $\approx 50\ \Omega\ \square^{-1}$. Subsequently, the masking layer was removed in a hydrofluoric acid solution etch. Similar processes of masking, photolithography, and diffusion were repeated to fabricate the phosphorus diffusion ($R_{sh} \approx 50\ \Omega\ \square^{-1}$) on the front of the wafer. After diffusion, the front and rear diffusion grid were defined through a masking layer using photolithography, then the diffusion between fingers were etched back and random pyramids were formed using KOH and a wetting agent RENA monoTEX.[44] After texturing, the wafer was cleaned in standard RCA solution and doped with light phosphorus diffusion with a sheet resistivity of $\approx 500\ \Omega\ \square^{-1}$. The masking stack was subsequently removed in concentrated HF. An optically and electrically optimized oxide-nitride-oxide layer is then deposited on both sides for surface passivation and anti-reflection.[45] After ONO deposition, the wafer was subjected to FGA at 400 °C for 30 min to activate the passivation. Contact opening was defined via photolithography, followed by etching of ONO layers via RIE and BHF. A metal stack consisting of Cr/Pd/Ag was evaporated on both sides of the wafer. Following the metal evaporation, the wafer was subjected to acetone ultrasonic bath in a metal lift-off process to remove unwanted metal, resulting in a finger width of ≈5 µm with a total front and rear contact area of 0.6% and 1.6%, respectively. Then the Cr/Pd/Ag contact was thickened with additional Ag by electroplating. Finally, the cells were subjected to a FGA annealing at 250 °C to improve contact adhesion and to lower the overall contact resistivity of the cell before being cut out to individual cells by laser processing for *JV* measurements.

Characterizations: The *JV* characteristic of the opaque perovskite cells was measured using solar simulator model #WAVELABS SINUS-220 equipped with a potentiostat source AutolabPGSTAT302N. The light intensity was calibrated at one Sun (100 mW cm^{-2}, AM1.5G) using the certified FraunhoferCalLab reference cell. Semi-transparent perovskite cells were measured in ambient using the same solar simulator and potentiostat. An opaque mask with an aperture of 0.25 cm^2 was used during the measurements. For large area semi-transparent cell, an opaque mask with an aperture of 1 cm^2 was used. Unless stated otherwise, the scan rate was fixed at 50 mV s^{-1} with a voltage step of 10 mV and dwell time of 200 ms. 4 cm^2 PERL silicon cells were measured using the same solar simulator and potentiostat under a 2.5 cm × 2.5 cm perovskite filter and a mask with an aperture of 4 cm^2 was used. 1 cm^2 PERL silicon cells were measured using the same solar simulator and potentiostat under a large area semi-transparent perovskite cell and a mask with an aperture of 1 cm^2 was used. XRD was performed with a D2 Phaser X-Ray Diffractometer with step size of 0.01° and integration time of 1s per step using Cu K_α as an X-ray source. Reflection/transmission was measured with a Lambda 1050 spectrophotometer (Perkin Elmer) in integrating sphere mode. SEM surface and cross-sectional images were taken using a FEI Verios scanning electron microscope (SEM) system. TEM analyses were performed using a JEOL 2100F instrument on perovskite films spun on the carbon side of the copper TEM grid. The AFM measurements were conducted in the nitrogen atmosphere using an Asylum Research Cypher ES (Oxford Instruments) instrument. The conducting Ti/Pt coated Si tip (Olympus AC240TM-R3) with a calibrated spring constant $k \approx 2.70$ N m^{-1} was employed for the measurement. TSC measurements were conducted in a closed cycle He cryostat using helium gas as the heat transfer medium. The atmosphere of the sample chamber was replaced with helium gas to make it inert. The possible traps were filled by illuminating a white LED array on the devices through an optical window for 5 min. After switching off the illumination, the device was kept in the dark for another 5 min to allow for thermalization of the carriers. Then, the device was heated up to room temperature with a constant rate of 7 K min^{-1}. The TSC signal was monitored using a sub-femtoamp source meter (Keithley-6430) during the heating. No external voltage was applied to measure the current and the built-in field was used to collect the de-trapped carriers. Time-resolved photoluminescence decay measurements were performed using LabRAM HR Evolution system with a time-correlated single photon counting system (DeltaPro-DD, Horiba). A 508 nm diode laser (DD-510L, Horiba) with pulse duration of 110 ps, µJ/fluence of ≈10 cm^2 $pulse^{-1}$, and a repetition rate of 312.5 kHz was used for excitation. ToF-SIMS was performed using a dual beam depth profiling with Cs^+ primary ions for the erosion (1 keV, 75 nA) and primary beam Bi_3^+ for the analysis (15 keV, 0.4 pA). XPS was conducted in an ultra-high vacuum apparatus from SPECS, which maintains a base pressure at low 10^{-10} mbar. The Mg $K\alpha$ line (12 kV, 200 W) was used for the measurements[46] with an UHV non-monochromatic X-ray source. The angle between the X-ray source and the analyser is 54°. Survey scan at a pass energy of 40 eV was processed first. High-resolution scans at a pass energy of 10 eV were then recorded for Mo, O, and C. UPS was applied to determine the occupied electron states of a sample surface[47] and the minimum energy required for an electron to escape the surface (secondary electron). In the measurement, electrons were emitted with a UV radiation of 21.218 eV excitation energy, and thus collected by detector. The UPS was operated with in situ XPS to avoid any contamination during sample transfer. IPES was used in this work for determining the unoccupied electron states of a sample,[48] which was based on electron in/photon out mechanism. In the experiment, a beam of electron with specified energy was directed onto a sample surface, entering the unoccupied states and releasing photon with corresponding energy. The photon was detected by ionizing gas phase of a mixed Ar/acetone inside a Geiger-Müller tube. As a function of the kinetic energy of the electrons, the emitted photons allowed comprising the IPES spectrum. By operating in situ IPES after UPS, a complete energy band structure of the sample was acquired. For determining the WF, the secondary electron cut-off on the binding energy scale of the UPS spectra was analyzed. The WF was taken by calculating the difference between the excitation energy of UV-light, which was 21.22 eV used for UPS, and the peak cut-off along the base line of the spectra. The value of valence band was determined by approximating the base line and the onset of valence electron peak of UPS with a linear curve and determining their intersections.[49] The same procedure was applied for determining the value of conductive band upon the conduction electron peak of IPES. When quantifying the peaks of XPS spectra, the intensity of peaks of various elements were normalized with atomic sensitive factor.[50] The stability of four-terminal perovskite silicon tandem solar cells was carried out under a white LED

© 2023 The Authors. Advanced Energy Materials published by Wiley-VCH GmbH

16146840, 0, Downloaded from https://onlinelibrary.wiley.com/doi/10.1002/aenm.202203607 by Karlsruher Inst F. Technologie, Wiley Online Library on [27/01/2023]. See the Terms and Conditions (https://onlinelibrary.wiley.com/terms-and-conditions) on Wiley Online Library for rules of use; OA articles are governed by the applicable Creative Commons License

light in ambient where the perovskite top cell was continuously tested and the silicon bottom cell was test unperiodically when the device was put under a simulated AM1.5G light.

Supporting Information

Supporting Information is available from the Wiley Online Library or from the author.

Acknowledgements

This work was supported by the Australian Government through the Australian Renewable Energy Agency (ARENA). Responsibility for the views, information, or advice expressed herein is not accepted by the Australian Government. Part of the experiment was performed at Australian National Fabrication Facility (ANFF) ACT Node. T.D. and J.Z. acknowledge the financial support of Postdoc Fellowships from the Australian Centre for Advanced Photovoltaics (ACAP). T.W. is the recipient of an Australian Research Council Future Fellowship (project number FT180100302) funded by the Australian Government. The financial support of this research through the Baden-Württemberg Foundation is acknowledged (project acronym: ANU-KIT-PV).

Open access publishing facilitated by Australian National University, as part of the Wiley - Australian National University agreement via the Council of Australian University Librarians.

Conflict of Interest

The authors declare no conflict of interest.

Data Availability Statement

The data that support the findings of this study are available from the corresponding author upon reasonable request.

Keywords

defects, perovskite solar cells, tandems, 2D perovskites

Received: October 24, 2022
Revised: December 14, 2022
Published online:

---

[1] Y. Zhao, F. Ma, Z. Qu, S. Yu, T. Shen, H.-X. Deng, X. Chu, X. Peng, Y. Yuan, X. Zhang, J. You, *Science* **2022**, *377*, 531.

[2] K. Yoshikawa, H. Kawasaki, W. Yoshida, T. Irie, K. Konishi, K. Nakano, T. Uto, D. Adachi, M. Kanematsu, H. Uzu, K. Yamamoto, *Nat. Energy* **2017**, *2*, 17032.

[3] Y. Yao, P. Hang, B. Li, Z. Hu, C. Kan, J. Xie, Y. Wang, Y. Zhang, D. Yang, X. Yu, *Small* **2022**, *18*, 2203319.

[4] a) W. Shockley, H. J. Queisser, *J. Appl. Phys.* **1961**, *32*, 510; b) S. P. Bremner, C. Yi, I. Almansouri, A. Ho-Baillie, M. A. Green, *Sol. Energy* **2016**, *135*, 750.

[5] G. E. Eperon, S. D. Stranks, C. Menelaou, M. B. Johnston, L. M. Herz, H. J. Snaith, *Energy Environ. Sci.* **2014**, *7*, 982.

[6] J.-W. Lee, D.-H. Kim, H.-S. Kim, S.-W. Seo, S. M. Cho, N.-G. Park, *Adv. Energy Mater.* **2015**, *5*, 1501310.

[7] a) M. Kim, G.-H. Kim, T. K. Lee, I. W. Choi, H. W. Choi, Y. Jo, Y. J. Yoon, J. W. Kim, J. Lee, D. Huh, H. Lee, S. K. Kwak, J. Y. Kim, D. S. Kim, *Joule* **2019**, *3*, 2179; b) H. Min, M. Kim, S.-U. Lee, H. Kim, G. Kim, K. Choi, J. H. Lee, S. I. Seok, *Science* **2019**, *366*, 749; c) G. Kim, H. Min, K. S. Lee, D. Y. Lee, S. M. Yoon, S. I. Seok, *Science* **2020**, *370*, 108; d) M. Jeong, I. W. Choi, E. M. Go, Y. Cho, M. Kim, B. Lee, S. Jeong, Y. Jo, H. W. Choi, J. Lee, J.-H. Bae, S. K. Kwak, D. S. Kim, C. Yang, *Nature* **2020**, *369*, 1615; e) J. J. Yoo, G. Seo, M. R. Chua, T. G. Park, Y. Lu, F. Rotermund, Y.-K. Kim, C. S. Moon, N. J. Jeon, J.-P. Correa-Baena, V. Bulović, S. S. Shin, M. G. Bawendi, J. Seo, *Nature* **2021**, *590*, 587; f) J. Jeong, M. Kim, J. Seo, H. Lu, P. Ahlawat, A. Mishra, Y. Yang, M. A. Hope, F. T. Eickemeyer, M. Kim, Y. J. Yoon, I. W. Choi, B. P. Darwich, S. J. Choi, Y. Jo, J. H. Lee, B. Walker, S. M. Zakeeruddin, L. Emsley, U. Rothlisberger, A. Hagfeldt, D. S. Kim, M. Grätzel, J. Y. Kim, *Nature* **2021**, *592*, 381; g) H. Min, D. Y. Lee, J. Kim, G. Kim, K. S. Lee, J. Kim, M. J. Paik, Y. K. Kim, K. S. Kim, M. G. Kim, T. J. Shin, S. Il Seok, *Nature* **2021**, *598*, 444.

[8] a) B. Conings, J. Drijkoningen, N. Gauquelin, A. Babayigit, J. D'Haen, L. D'Olieslaeger, A. Ethirajan, J. Verbeeck, J. Manca, E. Mosconi, F. D. Angelis, H.-G. Boyen, *Adv. Energy Mater.* **2015**, *5*, 1500477; b) W. Tan, A. R. Bowring, A. C. Meng, M. D. McGehee, P. C. McIntyre, *ACS Appl. Mater. Interfaces* **2018**, *10*, 5485; c) B. Brunetti, C. Cavallo, A. Ciccioli, G. Gigli, A. Latini, *Sci. Rep.* **2016**, *6*, 31896; d) M. J. Hong, S. R. Svadlenak, K. A. Goulas, J. G. Labram, *J. Phys. Mater.* **2019**, *3*, 014003.

[9] S.-H. Turren-Cruz, A. Hagfeldt, M. Saliba, *Science* **2018**, *362*, 449.

[10] Y. Hu, M. F. Aygüler, M. L. Petrus, T. Bein, P. Docampo, *ACS Energy Lett.* **2017**, *2*, 2212.

[11] T. Duong, Y. Wu, H. Shen, J. Peng, S. Zhao, N. Wu, M. Lockrey, T. White, K. Weber, K. Catchpole, *Sol. Energy Mater. Sol. Cells* **2018**, *188*, 27.

[12] S. Li, K. Fan, Y. Cui, S. Leng, Y. Ying, W. Zou, Z. Liu, C.-Z. Li, K. Yao, H. Huang, *ACS Energy Lett.* **2020**, *5*, 2015.

[13] a) S. Li, Z. Liu, Z. Qiao, X. Wang, L. Cheng, Y. Zhai, Q. Xu, Z. Li, K. Meng, G. Chen, *Adv. Funct. Mater.* **2020**, *30*, 2005846; b) L. Li, Y. Lv, Q. Liu, Z. Fan, R. Yuan, W. Tang, X. Liu, P. Zhang, W.-H. Zhang, *J. Mater. Chem. A* **2022**, *10*, 9161; c) S. Gharibzadeh, P. Fassl, I. M. Hossain, P. Rohrbeck, M. Frericks, M. Schmidt, T. Duong, M. R. Khan, T. Abzieher, B. A. Nejand, F. Schackmar, O. Almora, T. Feeney, R. Singh, D. Fuchs, U. Lemmer, J. P. Hofmann, S. A. L. Weber, U. W. Paetzold, *Energy Environ. Sci.* **2021**, *14*, 5875.

[14] B. Liu, H. Bi, D. He, L. Bai, W. Wang, H. Yuan, Q. Song, P. Su, Z. Zang, T. Zhou, J. Chen, *ACS Energy Lett.* **2021**, *6*, 2526.

[15] D. B. Khadka, Y. Shirai, M. Yanagida, T. Tadano, K. Miyano, *Adv. Energy Mater.* **2022**, *12*, 2202029.

[16] T. Bu, J. Li, H. Li, C. Tian, J. Su, G. Tong, L. K. Ono, C. Wang, Z. Lin, N. Chai, X.-L. Zhang, J. Chang, J. Lu, J. Zhong, W. Huang, Y. Qi, Y.-B. Cheng, F. Huang, *Science* **2021**, *372*, 1327.

[17] Z. Fan, Y. Yin, B. Cai, Q. Ma, Q. Liu, X. Liu, L. Yinhua, W.-H. Zhang, *Chem. Sci.* **2022**, *13*, 10512.

[18] S. Liu, R. Chen, X. Tian, Z. Yang, J. Zhou, F. Ren, S. Zhang, Y. Zhang, M. Guo, Y. Shen, Z. Liu, W. Chen, *Nano Energy* **2022**, *94*, 106935.

[19] a) J. Liu, M. De Bastiani, E. Aydin, G. T. Harrison, Y. Gao, R. R. Pradhan, M. K. Eswaran, M. Mandal, W. Yan, A. Seitkhan, M. Babics, A. S. Subbiah, E. Ugur, F. Xu, L. Xu, M. Wang, A. Rehman, A. Razzaq, J. Kang, R. Azmi, A. A. Said, F. H. Isikgor, T. G. Allen, D. Andrienko, U. Schwingenschlögl, F. Laquai, S. De Wolf, *Science* **2022**, *377*, 302; b) J. Xu, C. C. Boyd, Z. J. Yu, A. F. Palmstrom, D. J. Witter, B. W. Larson, R. M. France, J. Werner, S. P. Harvey, E. J. Wolf, W. Weigand, S. Manzoor, M. F. A. M. van Hest, J. J. Berry, J. M. Luther, Z. C. Holman, M. D. McGehee, *Science* **2020**, *367*, 1097.

16146840, 0, Downloaded from https://onlinelibrary.wiley.com/doi/10.1002/aenm.202203607 by Karlsruher Inst F. Technologie, Wiley Online Library on [27/01/2023]. See the Terms and Conditions (https://onlinelibrary.wiley.com/terms-and-conditions) on Wiley Online Library for rules of use; OA articles are governed by the applicable Creative Commons License

[20] a) C. G. Bischak, C. L. Hetherington, H. Wu, S. Aloni, D. F. Ogletree, D. T. Limmer, N. S. Ginsberg, *Nano Lett.* **2017**, *17*, 1028; b) E. T. Hoke, D. J. Slotcavage, E. R. Dohner, A. R. Bowring, H. I. Karunadasa, M. D. McGehee, *Chem. Sci.* **2015**, *6*, 613; c) T. Duong, H. K. Mulmudi, Y. Wu, X. Fu, H. Shen, J. Peng, N. Wu, H. T. Nguyen, D. Macdonald, M. Lockrey, T. P. White, K. Weber, K. Catchpole, *ACS Appl. Mater. Interfaces* **2017**, *9*, 26859.

[21] H. T. Pham, Y. Yin, G. Andersson, K. J. Weber, T. Duong, J. Wong-Leung, *Nano Energy* **2021**, *87*, 106226.

[22] a) T. Sugimoto, *Monodispersed Particles*, Elsevier, Amsterdam **2019**; b) Q. Gao, J. Qi, K. Chen, M. Xia, Y. Hu, A. Mei, H. Han, *Adv. Mater.* **2022**, *34*, 2200720.

[23] F. L. Binsbergen, *J. Polym. Sci.: Polym. Symp.* **1977**, *59*, 11.

[24] a) D. Prochowicz, R. Runjhun, M. M. Tavakoli, P. Yadav, M. Saski, A. Q. Alanazi, D. J. Kubicki, Z. Kaszkur, S. M. Zakeeruddin, J. Lewiński, M. Grätzel, *Chem. Mater.* **2019**, *31*, 1620; b) J. Chen, J. Xu, C. Zhao, B. Zhang, X. Liu, S. Dai, J. Yao, *ACS Appl. Mater. Interfaces* **2019**, *11*, 4597; c) H. Yu, F. Wang, F. Xie, W. Li, J. Chen, N. Zhao, *Adv. Funct. Mater.* **2014**, *24*, 7102.

[25] H. T. Pham, T. Duong, K. J. Weber, J. Wong-Leung, *ACS Mater. Lett.* **2020**, *2*, 415.

[26] K. P. McKenna, *ACS Energy Lett.* **2018**, *3*, 2663.

[27] W. Li, M. U. Rothmann, Y. Zhu, W. Chen, C. Yang, Y. Yuan, Y. Y. Choo, X. Wen, Y.-B. Cheng, U. Bach, J. Etheridge, *Nat. Energy* **2021**, *6*, 624.

[28] D. S. Lee, J. S. Yun, J. Kim, A. M. Soufiani, S. Chen, Y. Cho, X. Deng, J. Seidel, S. Lim, S. Huang, A. W. Y. Ho-Baillie, *ACS Energy Lett.* **2018**, *3*, 647.

[29] Z. Wang, Q. Lin, F. P. Chmiel, N. Sakai, L. M. Herz, H. J. Snaith, *Nat. Energy* **2017**, *2*, 17135.

[30] C.-T. Lin, J. Lee, J. Kim, T. J. Macdonald, J. Ngiam, B. Xu, M. Daboczi, W. Xu, S. Pont, B. Park, H. Kang, J.-S. Kim, D. J. Payne, K. Lee, J. R. Durrant, M. A. McLachlan, *Adv. Funct. Mater.* **2020**, *30*, 1906763.

[31] J.-W. Lee, Z. Dai, T.-H. Han, C. Choi, S.-Y. Chang, S.-J. Lee, N. De Marco, H. Zhao, P. Sun, Y. Huang, Y. Yang, *Nat. Commun.* **2018**, *9*, 3021.

[32] T. Duong, H. Pham, T. C. Kho, P. Phang, K. C. Fong, D. Yan, Y. Yin, J. Peng, M. A. Mahmud, S. Gharibzadeh, B. A. Nejand, I. M. Hossain, M. R. Khan, N. Mozaffari, Y. Wu, H. Shen, J. Zheng, H. Mai, W. Liang, C. Samundsett, M. Stocks, K. McIntosh, G. G. Andersson, U. Lemmer, B. S. Richards, U. W. Paetzold, A. Ho-Ballie, Y. Liu, D. Macdonald, A. Blakers, et al., *Adv. Energy Mater.* **2020**, *10*, 1903553.

[33] a) T. S. Sherkar, C. Momblona, L. Gil-Escrig, J. Ávila, M. Sessolo, H. J. Bolink, L. J. A. Koster, *ACS Energy Lett.* **2017**, *2*, 1214; b) J.-S. Park, J. Calbo, Y.-K. Jung, L. D. Whalley, A. Walsh, *ACS Energy Lett.* **2019**, *4*, 1321.

[34] a) R. Zheng, S. Zhao, H. Zhang, H. Li, J. Zhuang, X. Liu, H. Li, H. Wang, *Sol. Energy* **2021**, *224*, 472; b) T. Luo, G. Ye, X. Chen, M. Ding, T. Ye, C. Zhao, W. Zhang, H. Chang, *ACS Appl. Energy Mater.* **2021**, *4*, 12290; c) L. Zhang, Q. Kang, Y. Song, D. Chi, S. Huang, G. He, *Sol. RRL* **2021**, *5*, 2000681.

[35] J.-L. Bredas, *Mater. Horiz.* **2014**, *1*, 17.

[36] a) M. Morkel, L. Weinhardt, B. Lohmüller, C. Heske, E. Umbach, W. Riedl, S. Zweigart, F. Karg, *Appl. Phys. Lett.* **2001**, *79*, 4482; b) S. Gharibzadeh, B. A. Nejand, M. Jakoby, T. Abzieher, D. Hauschild, S. Moghadamzadeh, J. A. Schwenzer, P. Brenner, R. Schmager, A. A. Haghighirad, L. Weinhardt, U. Lemmer, B. S. Richards, I. A. Howard, U. W. Paetzold, *Adv. Energy Mater.* **2019**, *9*, 1803699.

[37] a) M. R. Khan, J. A. Schwenzer, J. Lehr, U. W. Paetzold, U. Lemmer, *J. Phys. Chem. Lett.* **2022**, *13*, 552; b) A. Baumann, S. Väth, P. Rieder, M. C. Heiber, K. Tvingstedt, V. Dyakonov, *J. Phys. Chem. Lett.* **2015**, *6*, 2350; c) C. Qin, T. Matsushima, T. Fujihara, W. J. Potscavage Jr., C. Adachi, *Adv. Mater.* **2016**, *28*, 466.

[38] J. Liu, J. Leng, K. Wu, J. Zhang, S. Jin, *J. Am. Chem. Soc.* **2017**, *139*, 1432.

[39] G. E. Eperon, M. T. Hörantner, H. J. Snaith, *Nat. Rev. Chem.* **2017**, *1*, 0095.

[40] a) Y. Chen, Z. Ying, X. Li, X. Wang, J. Wu, M. Wu, J. Sun, J. Sheng, Y. Zeng, B. Yan, X. Yang, J. Ye, *Nano Energy* **2022**, *100*, 107529; b) B. Tyagi, H. B. Lee, N. Kumar, W.-Y. Jin, K.-J. Ko, M. M. Ovhal, R. Sahani, H.-J. Chung, J. Seo, J.-W. Kang, *Nano Energy* **2022**, *95*, 106978; c) Y. Yao, P. Hang, B. Li, Z. Hu, C. Kan, J. Xie, Y. Wang, Y. Zhang, D. Yang, X. Yu, *Small* **2022**, *18*, 2203319.

[41] a) Y. Rong, Y. Hu, A. Mei, H. Tan, M. I. Saidaminov, S. I. Seok, M. D. McGehee, E. H. Sargent, H. Han, *Science* **2018**, *361*, eaat8235; b) J. Yan, T. J. Savenije, L. Mazzarella, O. Isabella, *Sustainable Energy Fuels* **2022**, *6*, 243.

[42] L. Shi, T. L. Young, J. Kim, Y. Sheng, L. Wang, Y. Chen, Z. Feng, M. J. Keevers, X. Hao, P. J. Verlinden, M. A. Green, A. W. Y. Ho-Baillie, *ACS Appl. Mater. Interfaces* **2017**, *9*, 25073.

[43] G. Coletti, S. L. Luxembourg, L. J. Geerligs, V. Rosca, A. R. Burgers, Y. Wu, L. Okel, M. Kloos, F. J. K. Danzl, M. Najafi, D. Zhang, I. Dogan, V. Zardetto, F. Di Giacomo, J. Kroon, T. Aernouts, J. Hüpkes, C. H. Burgess, M. Creatore, R. Andriessen, S. Veenstra, *ACS Energy Lett.* **2020**, *5*, 1676.

[44] W. Liang, T. Kho, J. Tong, P. Narangari, S. Armand, M. Ernst, D. Walter, S. Surve, M. Stocks, A. Blakers, K. C. Fong, *Sol. Energy Mater. Sol. Cells* **2021**, *222*, 110909.

[45] T. C. Kho, K. C. Fong, M. Stocks, K. McIntosh, E. Franklin, S. P. Phang, W. Liang, A. Blakers, *Prog. Photovoltaics* **2020**, *28*, 1034.

[46] a) K. Volgmann, F. Voigts, W. Maus-Friedrichs, *Surf. Sci.* **2012**, *606*, 858; b) S. Oswald, *Surf. Interface Anal.* **2010**, *42*, 1289.

[47] F. M. Spirkl, S. Kunz, F. F. Schweinberger, A. N. Farnbacher, R. Schroter, U. Heiz, *Rev. Sci. Instrum.* **2012**, *83*, 013114;

[48] a) S. Park, J. Jeong, G. Hyun, M. Kim, H. Lee, Y. Yi, *Sci. Rep.* **2016**, *6*, 35262; b) G. Krishnan, H. S. Al Qahtani, J. Li, Y. Yin, N. Eom, V. B. Golovko, G. F. Metha, G. G. Andersson, *J. Phys. Chem. C* **2017**, *121*, 28007.

[49] Y. Yin, D. A. Lewis, G. G. Andersson, *ACS Appl. Mater. Interfaces* **2018**, *10*, 44163.

[50] C. D. Wagner, *J. Electron Spectrosc. Relat. Phenom.* **1983**, *32*, 99.

© 2023 The Authors. Advanced Energy Materials published by Wiley-VCH GmbH

16146840, 0, Downloaded from https://onlinelibrary.wiley.com/doi/10.1002/aenm.202203607 by Karlsruher Inst F. Technologie, Wiley Online Library on [27/01/2023]. See the Terms and Conditions (https://onlinelibrary.wiley.com/terms-and-conditions) on Wiley Online Library for rules of use; OA articles are governed by the applicable Creative Commons License